Supplement of Atmos. Chem. Phys., 24, 12595–12621, 2024
https://doi.org/10.5194/acp-24-12595-2024-supplement

Atmospheric Chemistry and Physics
Open Access
EGU

Supplement of

The annual cycle and sources of relevant aerosol precursor vapors in the central Arctic during the MOSAiC expedition

Matthew Boyer et al.

Correspondence to: Matthew Boyer (matthew.boyer@helsinki.fi) and Tuija Jokinen (t.jokinen@cyi.ac.cy)

Supplemental Information

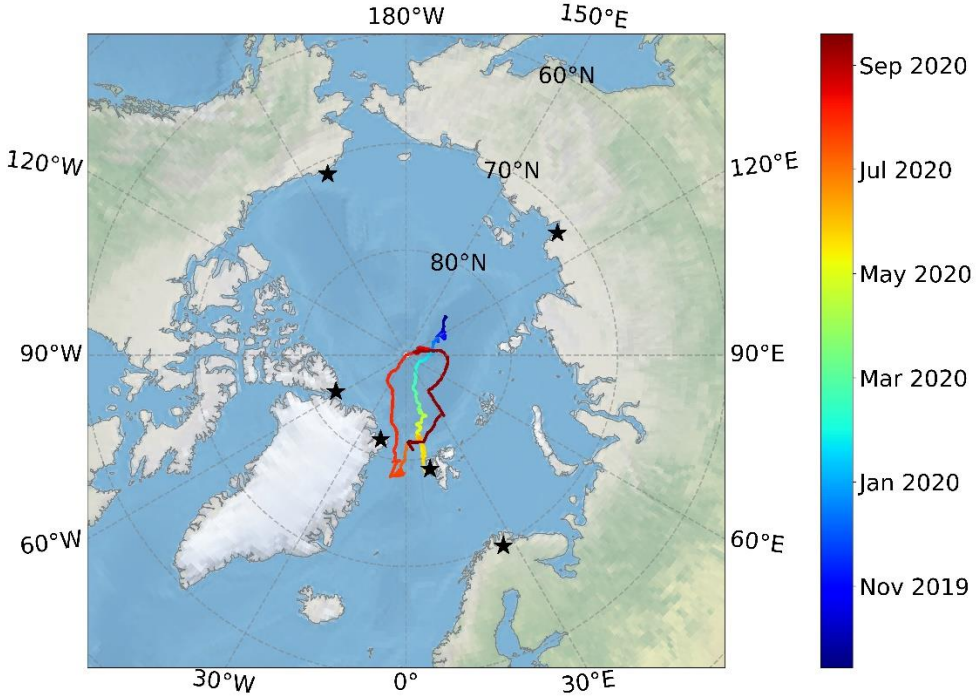

Figure S1. The location of *Polarstern* during the MOSAiC expedition. The color bar shows the time of year. Adapted from Boyer et al. (2023).

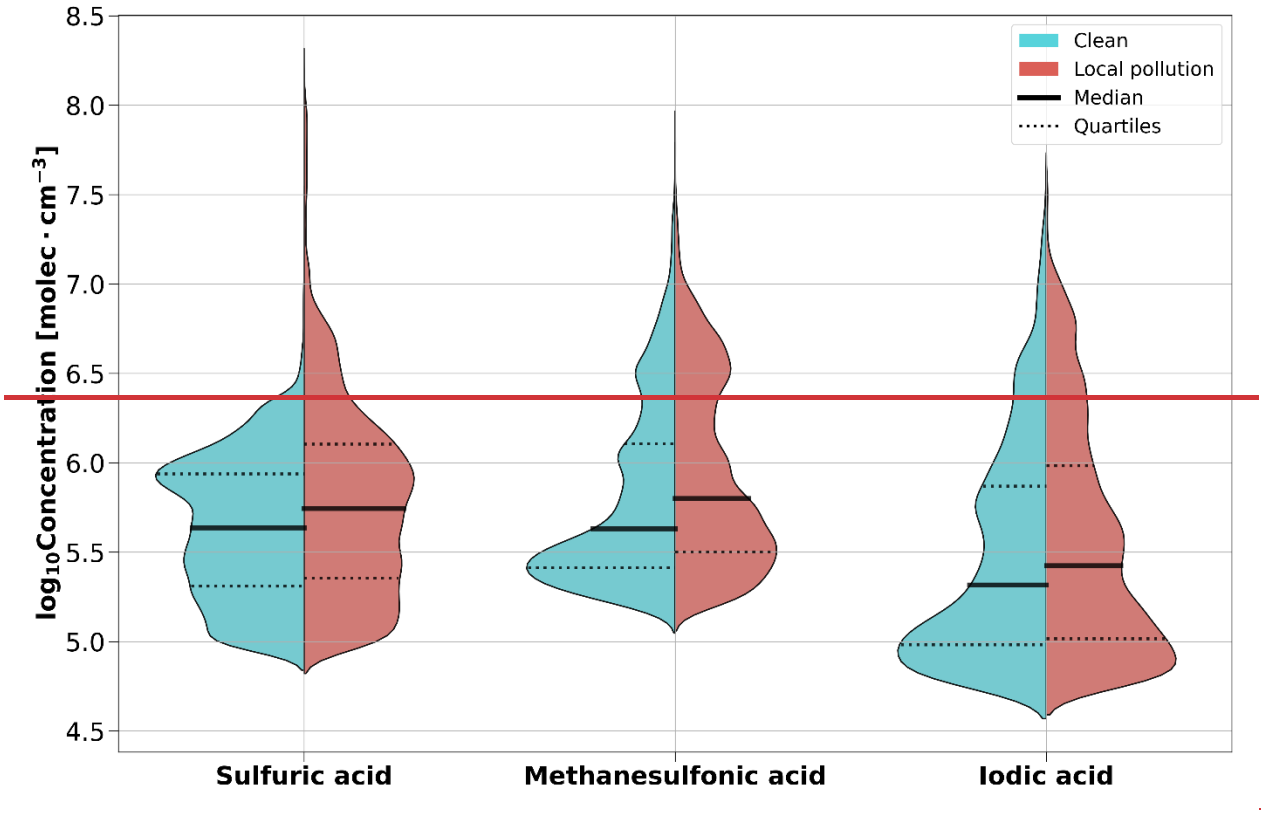
8.5
8.0
7.5
7.0
6.5
6.0
5.5
5.0
4.5
log10Concentration [molec · cm−3]
Clean
Local pollution
Median
Quartiles
Sulfuric acid
Methanesulfonic acid
Iodic acid

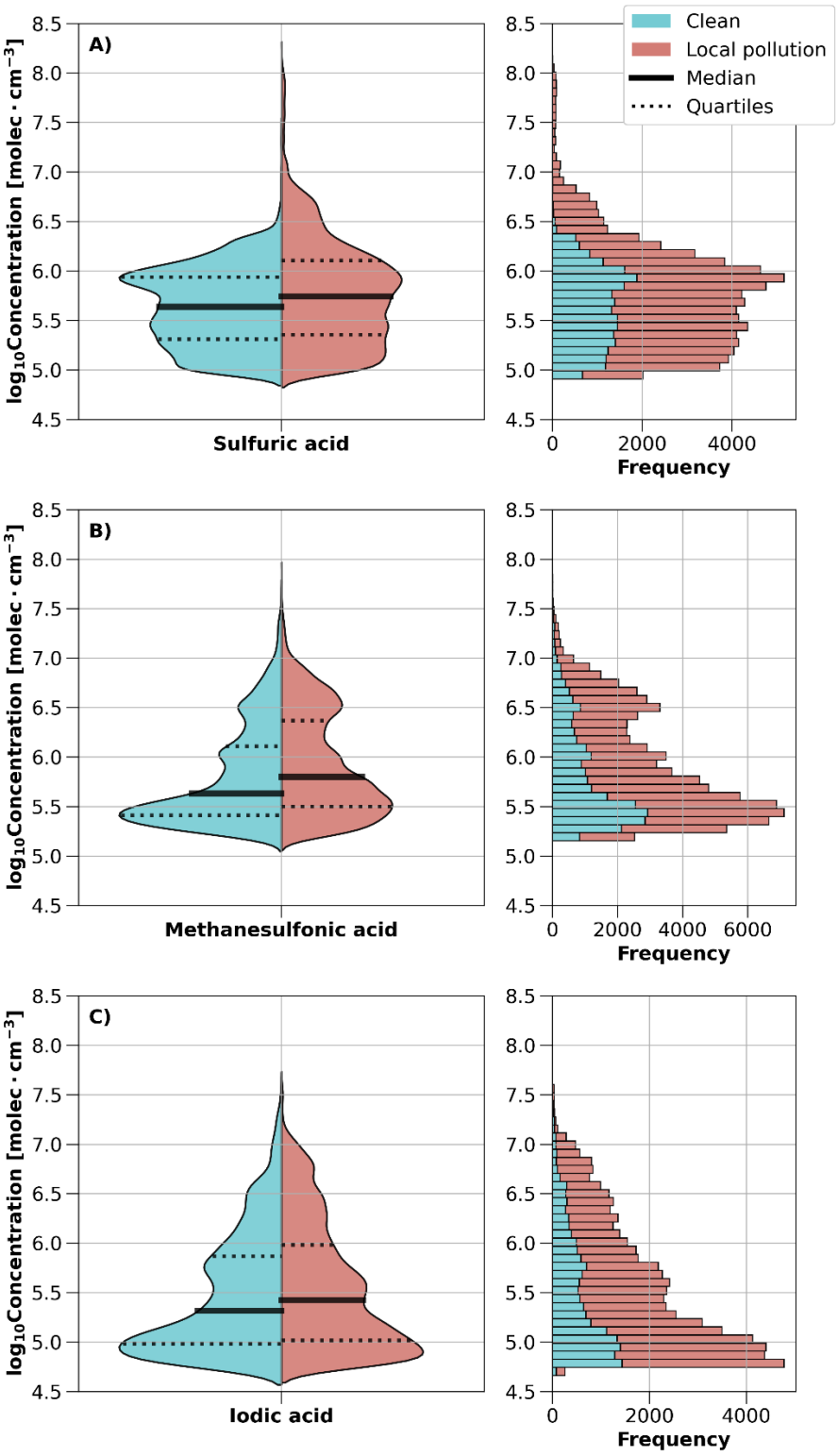

Figure S2. The influence of local pollution on the ~~gas phase~~aerosol precursor vapor concentrations~~.~~ ~~of SA, MSA, and IA.~~ The violins show the ~~frequency~~ distribution of the gas phase concentration for the clean (blue) and polluted (red) periods to evaluate the influence of local pollution, from the ship and logistical activities, on A) SA, B) MSA, and C) IA ~~each species~~ during the campaign. The medians and interquartile ranges of each data subset are represented by the solid and dashed black lines, respectively. Since the distributions of the violins are normalized by the number of observations, the corresponding frequencies of the observations are included for clarity.

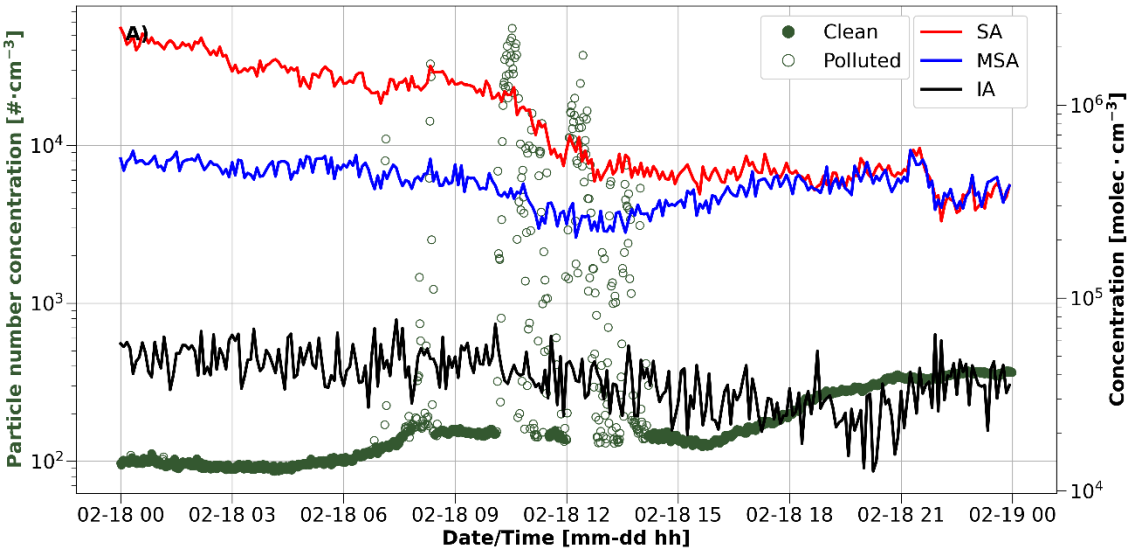

Figure S3. A single-day comparison of particle number and aerosol precursor vapor concentration timeseries during clean and polluted periods. The particle number concentrations during clean periods are shown with solid green circles, whereas the periods identified as local pollution are indicated by hollow green circles. The red, blue, and black lines correspond to the concentrations of SA, MSA, and IA, respectively. The reported particle number concentrations were measured with a condensation particle counter (TSI 3025), which was also used to identify local pollution using the pollution detection algorithm described in Beck et al. (2022).

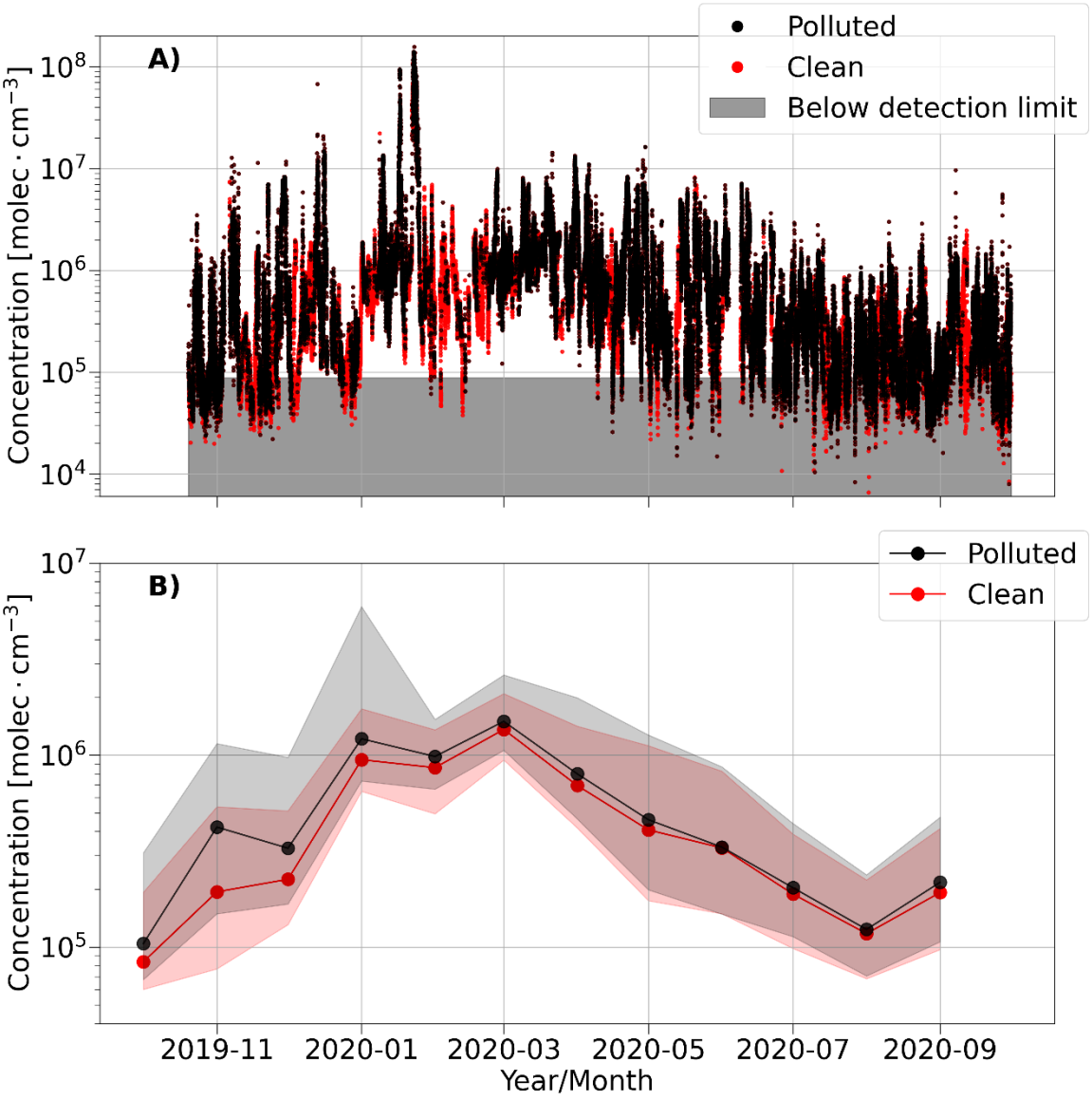

Figure S4. Comparison of sulfuric acid concentrations during clean and polluted periods. A) The timeseries of SA concentration at 5-minute resolution color coded according to polluted (black) and clean (red) periods. The polluted periods are influenced by local pollution from the ship stack, as identified by a pollution detection algorithm (Beck et al., 2022) applied to particle concentrations from a condensation particle counter (TSI, model 3025) that was collocated with the NO_3-CIMS in the *Swiss* container. The dark gray shaded region shows the concentrations that are below the determined SA detection limit. B) The monthly median concentrations for polluted (black) and clean (red) periods. The shaded regions show the interquartile range for each respective period. Note that the interquartile ranges in this figure also include the concentrations below the detection limit.

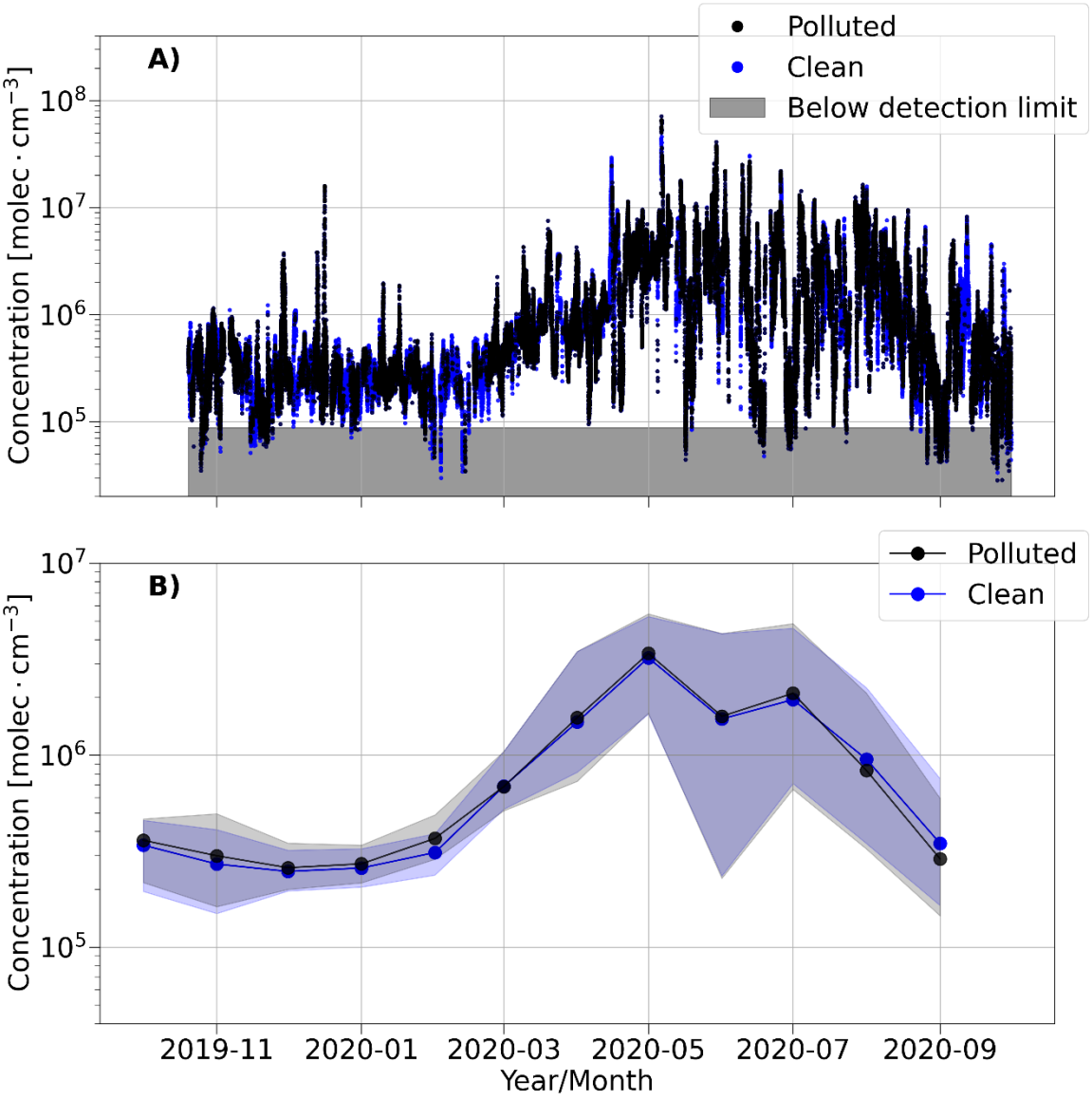

Figure S5. Comparison of methanesulfonic acid concentrations during clean and polluted periods. A) The timeseries of MSA concentration at 5-minute resolution color coded according to polluted (black) and clean (blue) periods. The polluted periods are influenced by local pollution from the ship stack, as identified by a pollution detection algorithm (Beck et al., 2022) applied to particle concentrations from a condensation particle counter (TSI, model 3025) that was collocated with the NO_3-CIMS in the *Swiss* container. The dark gray shaded region shows the concentrations that are below the determined MSA detection limit. B) The monthly median concentrations for polluted (black) and clean (blue) periods. The shaded regions show the interquartile range for each respective period. Note that the interquartile ranges in this figure also include the concentrations below the detection limit.

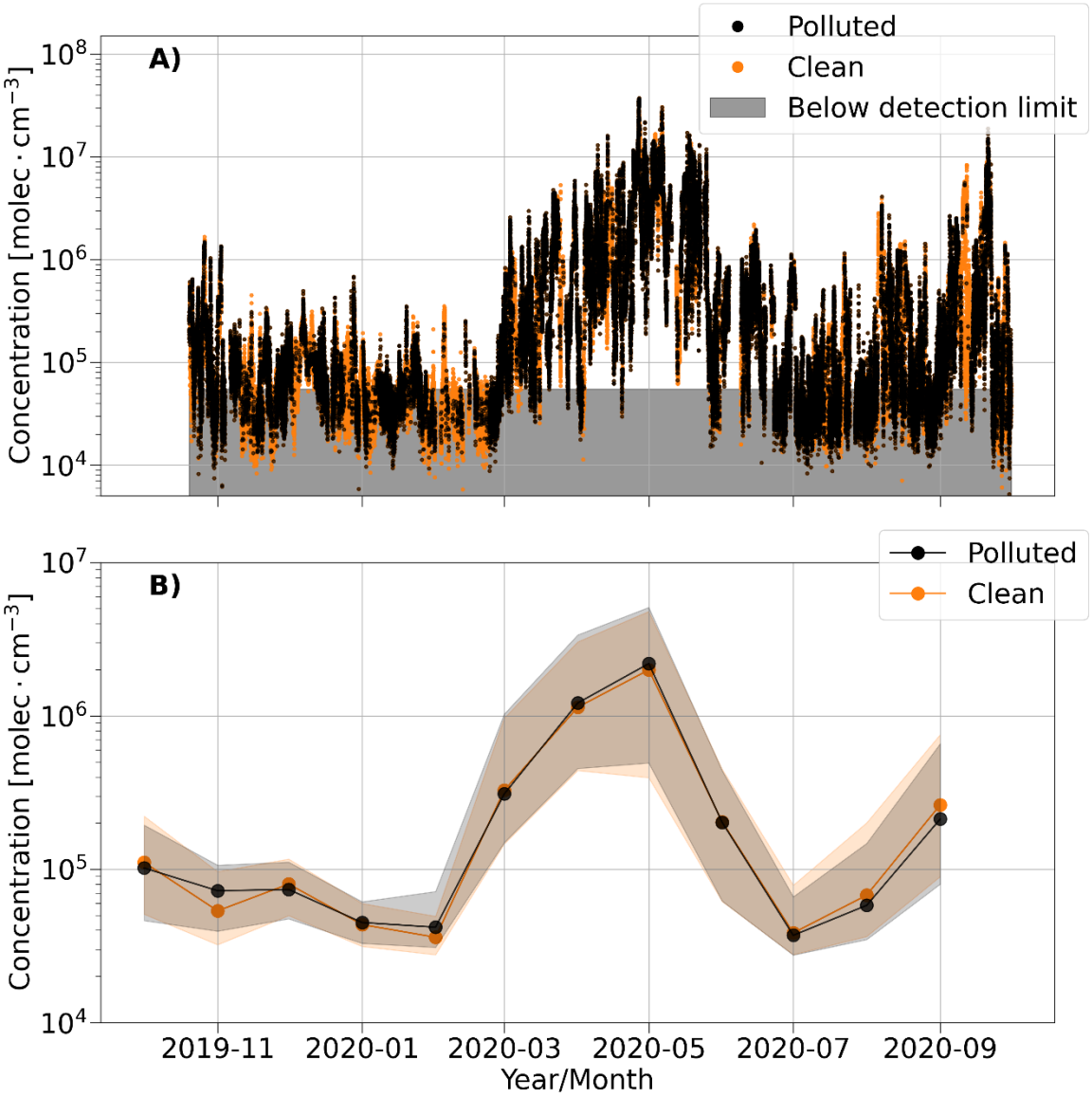

Figure S6. Comparison of iodic acid concentrations during clean and polluted periods. A) The timeseries of IA concentration at 5-minute resolution color coded according to polluted (black) and clean (orange) periods. The polluted periods are influenced by local pollution from the ship stack, as identified by a pollution detection algorithm (Beck et al., 2022) applied to particle concentrations from a condensation particle counter (TSI, model 3025) that was collocated with the NO_3-CIMS in the *Swiss* container. The dark gray shaded region shows the concentrations that are below the determined IA detection limit. B) The monthly median concentrations for polluted (black) and clean (red) periods. The shaded regions show the interquartile range for each respective period. Note that the interquartile ranges in this figure also include the concentrations below the detection limit.

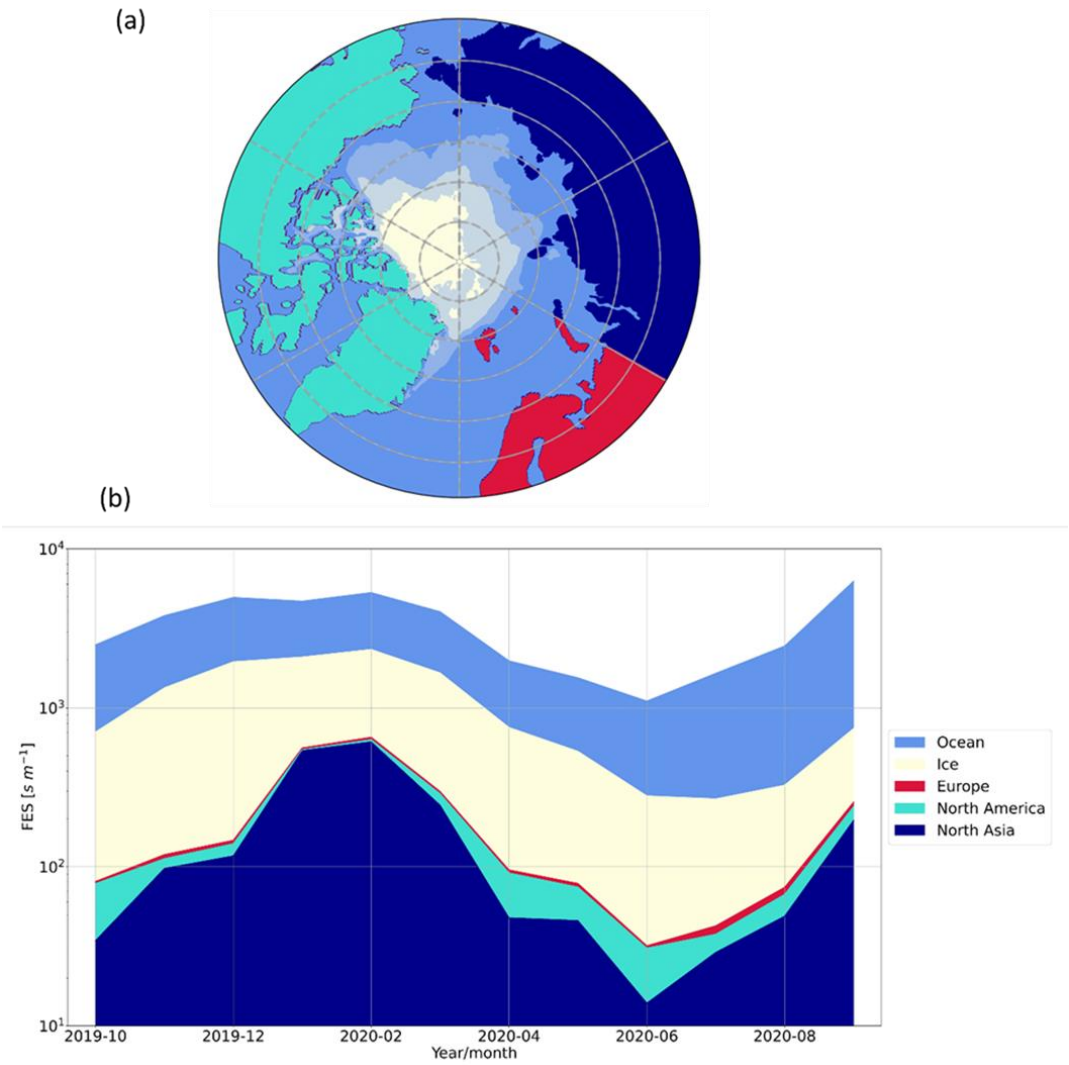

Figure S7. The seasonality of surface influence from air mass source regions using FLEXPART. A geographical mask (a) was applied to the FLEXPART air tracer data to quantify the FES associated with each geographical source region (b). The FES was determined from the FLEXPART air tracer data within the lowest 100 meters of the atmosphere and was used to identify the influence of different source regions on the observed aerosol throughout the year. Taken from Boyer et al. (2023).

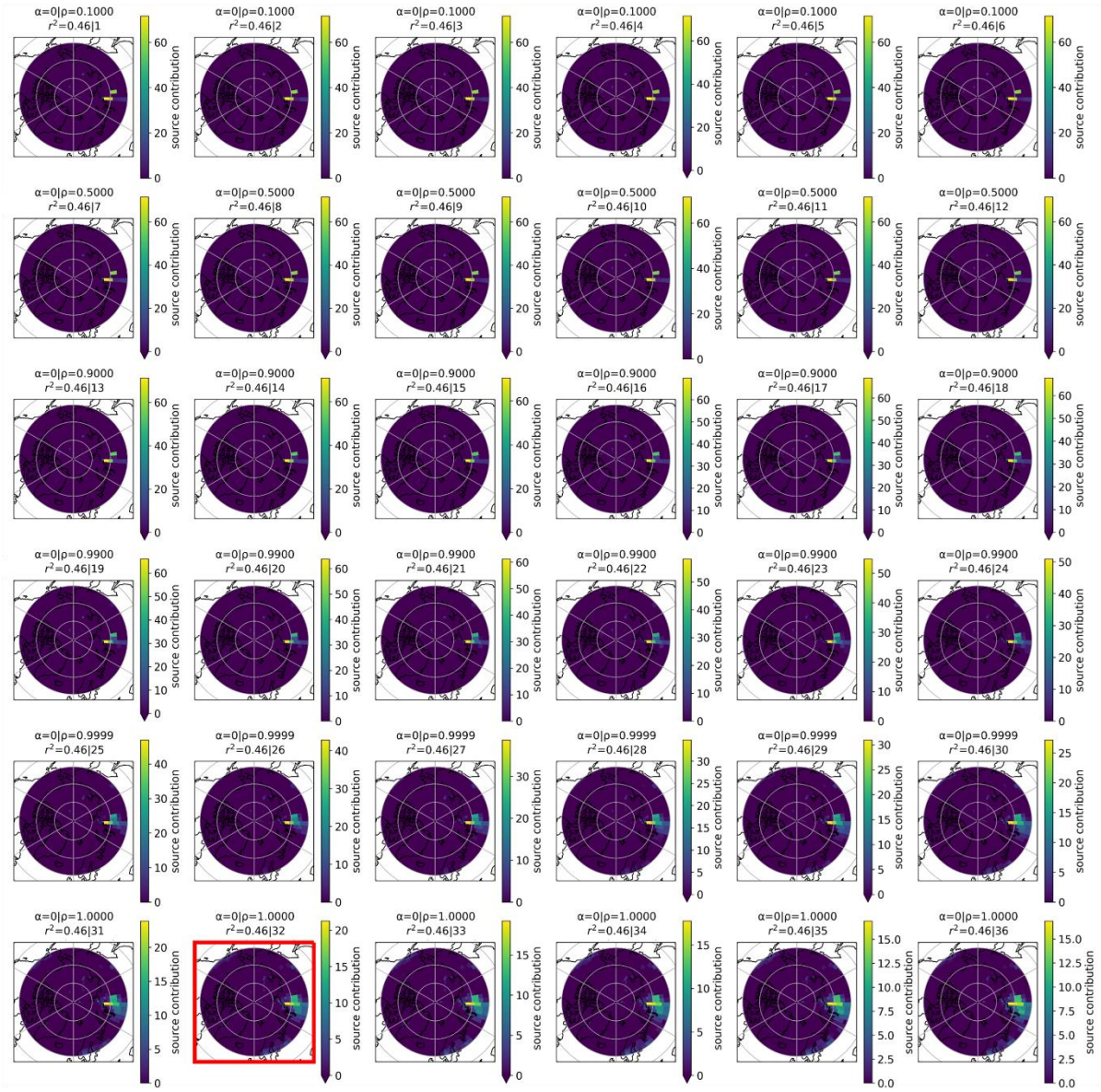

Figure S8. The 36 source region footprint maps of SO_2 produced using the iterative elastic net regularization method in the inverse model. The polygons represent the source region locations identified by the inverse model for various levels of penalization in the elastic net regression method. The elastic net regularization parameters α and ρ, as described in Section 2.6, are included above each map, as well as the correlation coefficient (r^2) and the iteration number. Iteration 32, outlined in red, was selected in this analysis as it represents known source regions while minimizing noisy regions.

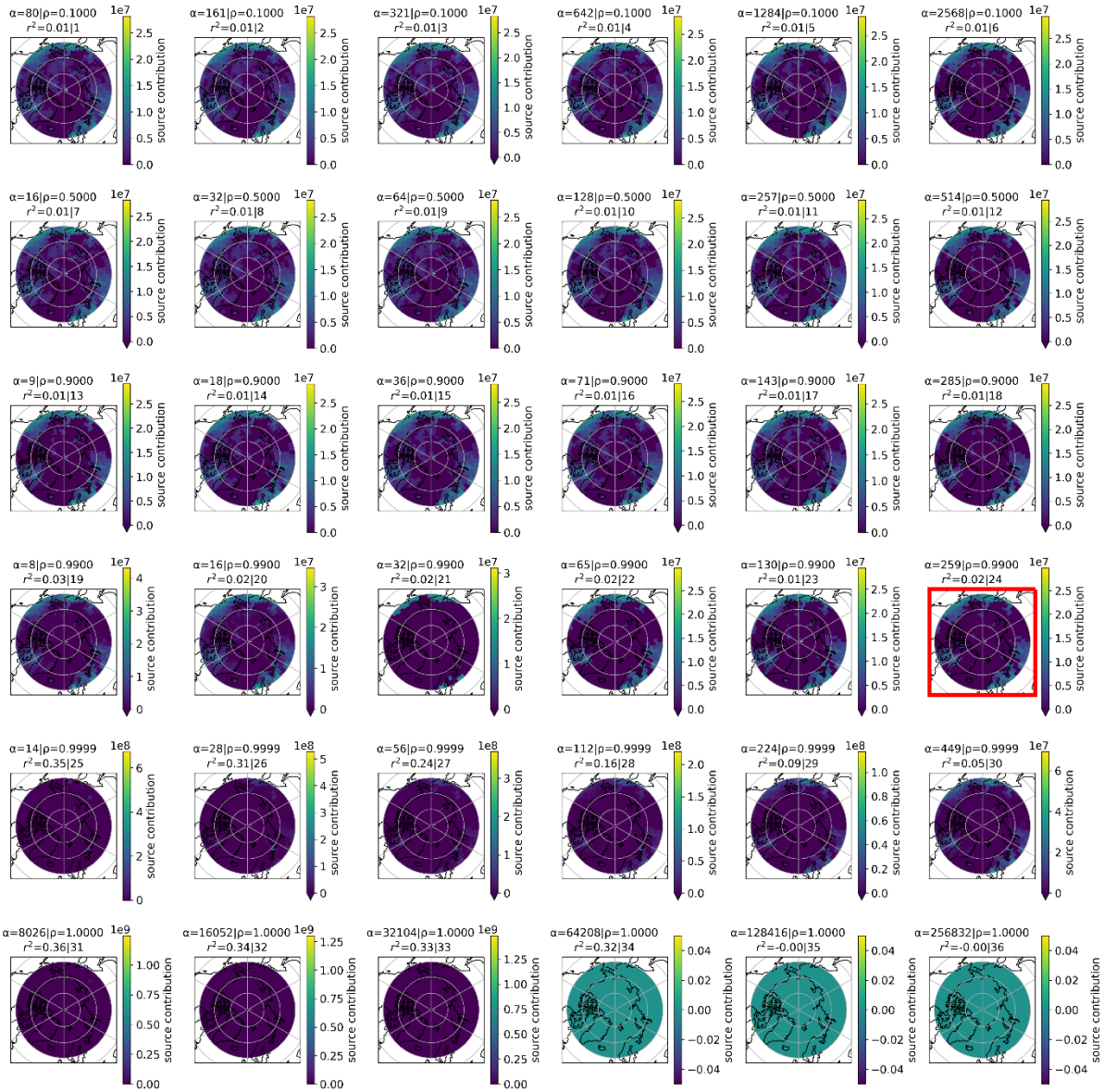

Figure S9. The 36 source region footprint maps of SA produced using the iterative elastic net regularization method in the inverse model. The polygons represent the source region locations identified by the inverse model for various levels of penalization in the elastic net regression method. The elastic net regularization parameters α and ρ, as described in Section 2.6, are included above each map, as well as the correlation coefficient (r^2) and the iteration number. The Iteration 24, outlined in red, was selected in this analysis as it represents known source regions while minimizing noisy regions.

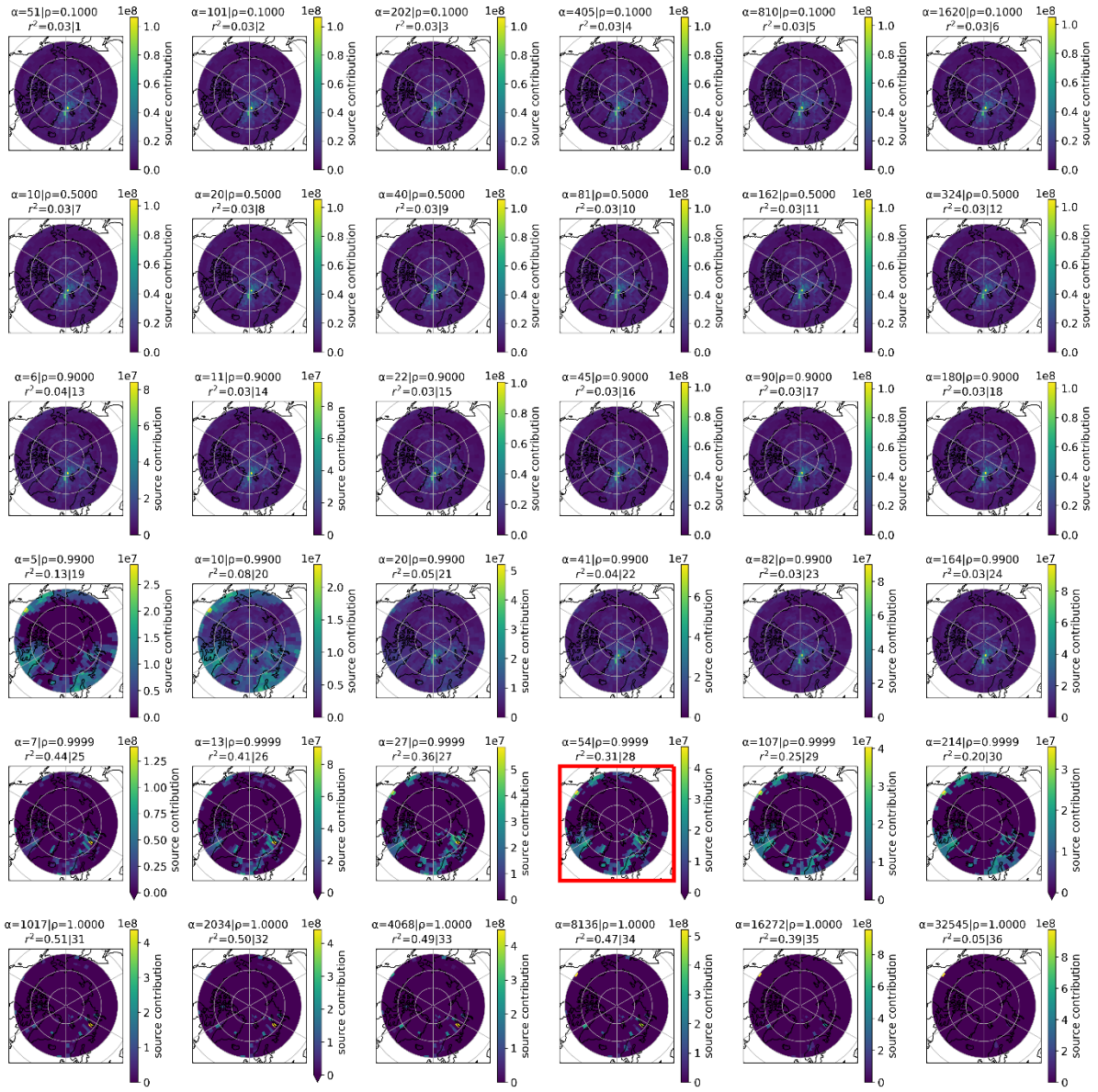

Figure S10. The 36 source region footprint maps of MSA produced using the iterative elastic net regularization method in the inverse model. The polygons represent the source region locations identified by the inverse model for various levels of penalization in the elastic net regression method. The elastic net regularization parameters α and ρ, as described in Section 2.6, are included above each map, as well as the correlation coefficient (r^2) and the iteration number. Iteration 28, outlined in red, was selected in this analysis as it represents known source regions while minimizing noisy regions.

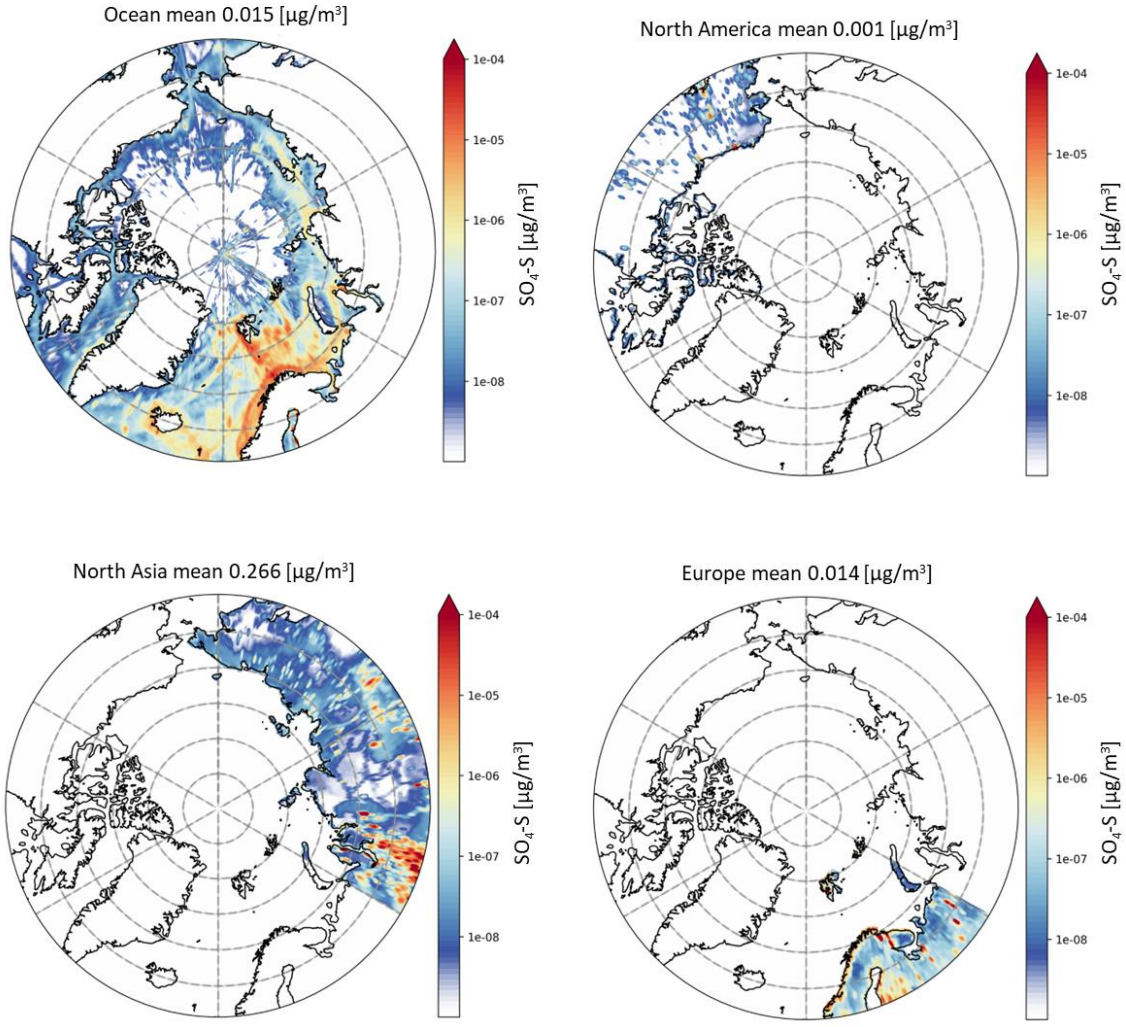

Figure S11. Annual average source contribution maps of SO_4-S by source region from the ECLIPSE v6b emission inventory. The SO_4-S concentrations, or anthropogenic particulate sulfate mass derived from SO_2 emissions, are presented as the yearly averages according to different geographic source regions.

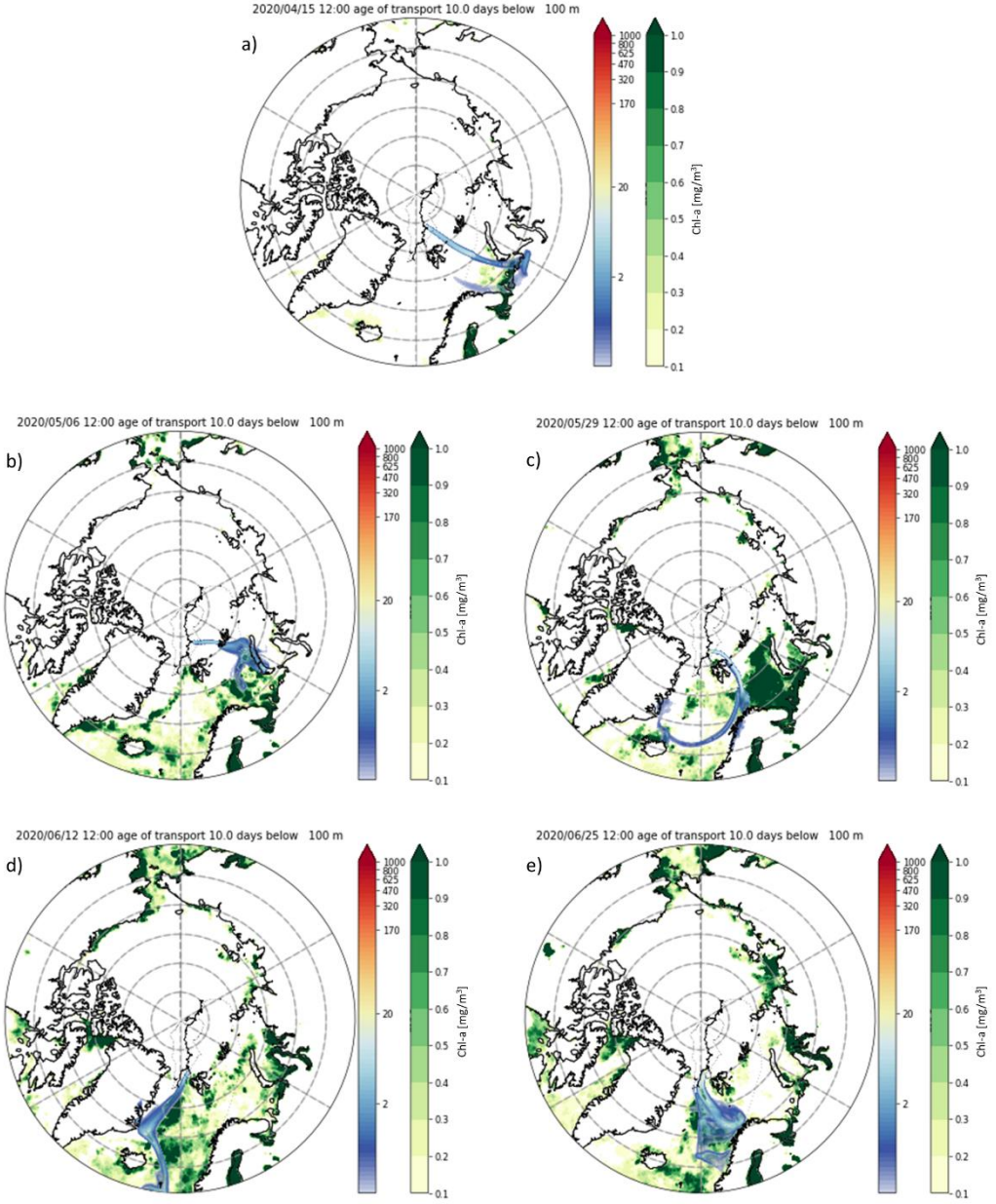

Figure S12. FLEXPART trajectories coupled with chl-a concentrations. Maps of individual, 10-day air mass trajectories in the lower 100 m altitude for a) April 15, 2020; b) May 06, 2020; c) May 29, 2020; d) June 12, 2020; and e) June 25, 2020 are shown with the chl-a concentrations (green colorbar) from the OC-CCI dataset. The air tracer is indicated by the blue-red colorbar.

Table S1. Monthly statistics for the aerosol precursor vapors measured during MOSAiC. The statistics include the monthly median, 25th and 75th percentiles, and the maximum values for SA, MSA, and IA. The monthly percentage of data influenced by local pollution sources is also included. For readability, all units in concentration (molec·cm^{-3}), are scaled by 1e+05, except for pollution, which is given as a percentage.

Time	SA				MSA				IA				Percentage pollution
	Median	25th percentile	75th percentile	Maximum	Median	25th percentile	75th percentile	Maximum	Median	25th percentile	75th percentile	Maximum	
October 2019	0.84	0.6	1.93	34.9	3.4	1.95	4.58	11.5	1.11	0.51	2.22	16.7	75
November 2019	1.94	0.77	5.38	128	2.71	1.5	4.09	37.4	0.54	0.32	0.96	13.5	56
December 2019	2.26	1.31	5.13	674	2.48	1.96	3.2	159	0.8	0.5	1.17	6.85	38
January 2020	9.47	6.48	17.4	157	2.59	2.06	3.26	19.7	0.44	0.31	0.6	3.51	47
February 2020	8.61	4.95	13.5	98.9	3.11	2.37	3.9	22.6	0.36	0.28	0.49	4.37	34
March 2020	13.6	9.42	20.9	143	6.88	5.23	10.4	75.2	3.27	1.46	9.68	58.8	73
April 2020	6.95	4.18	14.2	164	14.9	8.15	34.6	294	11.4	4.4	30.4	373	77
May 2020	4.08	1.75	11.2	82	32.1	16.3	52.7	712	20	3.95	48	305	79
June 2020	3.29	1.49	8.25	71.2	15.4	2.35	42.9	306	2.04	0.62	4.49	22	86
July 2020	1.89	0.98	3.88	29.3	19.5	7.12	45.8	164	0.39	0.28	0.79	11.5	80
August 2020	1.18	0.69	2.24	30.1	9.51	3.46	22.4	158	0.68	0.36	2.01	41.1	69
September 2020	1.93	0.97	4.15	96.1	3.47	1.65	7.55	82.1	2.63	0.9	7.55	188	66

References

Beck, I., Angot, H., Baccarini, A., Dada, L., Quéléver, L., Jokinen, T., Laurila, T., Lampimäki, M., Bukowiecki, N., Boyer, M., Gong, X., Gysel-Beer, M., Petäjä, T., Wang, J., and Schmale, J.: Automated identification of local contamination in remote atmospheric composition time series, Atmospheric Meas. Tech., 15, 4195–4224, https://doi.org/10.5194/amt-15-4195-2022, 2022.

Boyer, M., Aliaga, D., Pernov, J. B., Angot, H., Quéléver, L. L. J., Dada, L., Heutte, B., Dall'Osto, M., Beddows, D. C. S., Brasseur, Z., Beck, I., Bucci, S., Duetsch, M., Stohl, A., Laurila, T., Asmi, E., Massling, A., Thomas, D. C., Nøjgaard, J. K., Chan, T., Sharma, S., Tunved, P., Krejci, R., Hansson, H. C., Bianchi, F., Lehtipalo, K., Wiedensohler, A., Weinhold, K., Kulmala, M., Petäjä, T., Sipilä, M., Schmale, J., and Jokinen, T.: A full year of aerosol size distribution data from the central Arctic under an extreme positive Arctic Oscillation: insights from the Multidisciplinary drifting Observatory for the Study of Arctic Climate (MOSAiC) expedition, Atmospheric Chem. Phys., 23, 389–415, https://doi.org/10.5194/acp-23-389-2023, 2023.